19th Brazilian Congress of Thermal Sciences and Engineering
November 06th-10th, 2022, Bento Gonçalves - RS - Brazil

ENCIT2022-0463
PIV INVESTIGATION OF THE FLOW FIELD IN A CENTRIFUGAL ROTOR

Edgar Minoru Ofuchi
Henrique Stel
Ernesto Mancilla
Rigoberto E. M. Morales
Multiphase Flow Research Center – NUEM, Graduate Program in Mechanical and Materials Engineering – PPGEM, Federal University of Technology of Paraná, Curitiba, PR, Brazil
edgarofuchi@alunos.utfpr.edu.br
stel.henrique@gmail.com
faermara@gmail.com
rmmorales@utfpr.edu.br

Abstract. *This work aims to present an investigation of the flow field in a centrifugal rotor employing two-dimensional Particle Image Velocimetry (PIV) at different planes for different rotating speeds and flow rate operations. The rotor prototype has equal inlet and outlet blade angles and is constructed to have a quasi-2D geometry. The PIV measurements were performed using the phase-locking technique, in which 500 samples were acquired in each experiment. The result for the head coefficient as a function of the flow coefficient shows that the centrifugal rotor prototype behaves according to pump laws. From the analysis conducted at different planes, it could be observed that for the best efficiency point flow rate and above, the velocity field is blade aligned, while for part-load operation, a strong separation is observed. Moreover, velocity is higher near the hub, while turbulence intensities are higher near the shroud for* Q_{BEP} *and above. This difference can be attributed to the change in the flow direction from the development pipe to the rotor channels.*

Keywords: *centrifugal pump, PIV, turbulence intensity.*

1. INTRODUCTION

Centrifugal pumps are widely used to transport fluid in different areas such as the oil and gas sector, medical industry, and chemical plants. The flow inside a centrifugal pump is generally turbulent, complex, and unstable under certain operating conditions. Understanding the complex flow pattern inside a centrifugal pump can contribute to a better design, for instance, to reduce vibration and hydraulic losses (Si et al., 2019; Tong et al., 2020). Moreover, understanding the flow behavior can provide valuable information on the pump performance, such as how the different hydraulic losses contribute to the overall performance (Vieira et al., 2015).

In this sense, different techniques have been employed to obtain information on the flow in a centrifugal pump, e.g., Computational Fluid Dynamics (CFD), Particle Image Velocimetry (PIV), and Laser Doppler Velocimetry (LDV), among others (Feng et al., 2009; Li et al., 2020; Ofuchi et al., 2017; Pedersen et al., 2003; Posa and Lippolis, 2019). Generally, the authors are interested in analyzing the flow pattern inside the rotor channels at different operating conditions and how it affects the flow field, turbulence, Reynolds shear stress, and overall performance. For instance, Stel et al. (2015) performed U-RANS (Unsteady Reynolds Averaged Navier-Stokes) simulations in a multistage centrifugal pump. They observed that the flow field in the first stage is different from the following stages, which could be due to better inlet flow orientation. The authors also observed recirculation in the diffuser at part-load operation.

Experimental measurements of the flow field are possible with velocity probes such as hot-wire or LDV. However, it has the disadvantage of measuring only a single point. On the other hand, the PIV technique allows for measuring a significant area of the flow field and has been used over the past decades showing to be a reliable technique. For example, Feng et al. (2010), Li et al. (2017), and Sinha et al. (2000) studied the interaction between impeller and diffuser, where the authors could observe wake interactions in both impeller and diffuser channels. Flow interaction between impeller and volute was also investigated by Keller et al. (2014) and Zhang et al. (2018), in which the authors could observe that the blade–tongue interactions are dominated by high vortex shedding from the impeller blades. They also noted that vortex impingement and on the tongue tip induce distortion and fragmentation of the vortex structures. In part-load operations,

diverse flow interactions occur, such as flow separation and recirculation. These interactions lead to a stall cell formation showing a blockage effect on the rotor leading to an increase in pressure and velocity fluctuations (Pedersen et al., 2003; Sinha et al., 2001). Moreover, the so-called two-channel flow pattern is formed, which implies different flow behaviors in the rotor channels (Feng et al., 2010b; Pedersen et al., 2003).

Flow visualization inside a centrifugal pump has many challenges to overcome. The commercial pumps have thick metallic casings, curved channels, and generally restricted visual access. These factors make it challenging to perform PIV measurements, especially in different rotor axial planes. Most studies only measure the flow field at a midspan location, which could lack information about the flow pattern in the rotor channels. Furthermore, the large number of degrees of freedom for constructing a centrifugal pump, such as leading angle and blade height, makes existing studies almost unique.

In this sense, this study presents a PIV investigation of the flow field in a prototype centrifugal rotor to characterize the flow field at different rotating speeds and flow rates for various measurement planes. The rotor model is fully transparent, providing good visualization of the flow field, and the cylindrical blade geometry allows reliable measurement of the flow field through planar PIV. First, it is presented the head curve for different rotating speeds. Then, it is shown that kinetic similarity holds for different variables (velocity, turbulence intensity, and Reynolds shear stress). Next, an analysis of the flow field in different channels is presented. Finally, the flow field is evaluated at different planes for different flow rates. We expect that the outcomes from this work can be helpful for a better understanding of the flow in a centrifugal rotor with a vaneless diffuser.

2. EXPERIMENTAL SETUP

An experimental loop was designed to perform the visualization inside a transparent rotor prototype. Figure 1 presents a schematic of this experimental setup, which is based on the one employed by Stel et al. (2020) with some adjustments to perform PIV experiments. The working fluid was tap water at ambient temperature (25ºC).

A booster pump provides water through the loop, while a Coriolis flowmeter measures the flow rate before entering the development pipe, which has a 17·Din length (Din = 70mm), where Din is the pipe's inner diameter. Then, the flow enters the test rotor, where PIV measurements were performed. An unvaned discharge chamber collects the flow before it returns to the water tank through the return lines. It is composed of two PMMA parts with an outer radius of 330 mm, and a height of 105mm.

The booster pump and two valves in the primary and secondary return lines control the flow rate and the impeller inlet pressure. Two differential pressure sensors and a Coriolis flow meter are used to measure the intake pressure, the pressure gain of the rotor, and the liquid mass flow rate with uncertainties of ±15.7 Pa and ± 0.0016 m³/h, as described Stel et al. (2020). A dynamic sealing composed of two metal rings and two lip seals fixed around the rotor periphery is used to avoid fluid loss at the rotor/discharge chamber interface, eliminating the need to enclose the rotor with a carcass. Details of the loop system can be found in Stel et al. (2020).

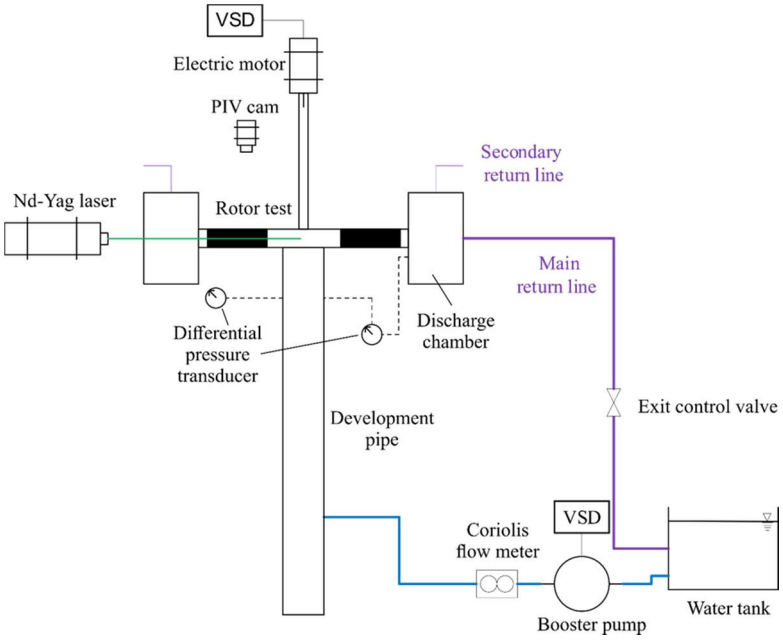

Figure 1 – Experimental loop

The closed rotor prototype constructed to perform the experiments is made out of polymethyl methacrylate (PMMA). This rotor is equivalent to the one used by Stel et al. (2020). The difference is the PMMA material used, allowing the laser sheet from the PIV system to pass through. In addition, the channel height has increased to 10.8mm, as well as the hub and shroud thickness to 20mm for including metal rings that slide against the lip seals. Figure 2 shows a picture of the rotor prototype and a scheme with its main dimensions. This quasi-2D geometry was constructed to reduce the influence of 3D flow and provide better flow visualization.

The rotor design flow rate (Q_{Des}) is the condition where the liquid flows perfectly aligned with the rotor's blade. It is used as a reference in the following sections to calculate the flow rate at the best efficiency point (BEP) for different rotating speeds. An algebraic expression for Q_{Des} based on a perfect approach flow alignment (CFD calculations confirmed this in a quasi-2D simulation, Stel et al. (2020b) is given by the following equation:

$$Q_{Des} = \left(\pi R_1\right)/_{15} \cdot b \cdot n_{Des} \cdot \tan\left(\beta_1\right) \tag{1}$$

in which, n_{Des} is the design rotating speed in rpm, b is the blade height, R1 is the blade leading edge radius, and β_1 is the blade leading edge angle. Assuming a design rotating speed of 1000 rpm, the design flow rate and head are Q_{Des} = 0.003411 m³/s (12.267 m³/h or 54.01 US gpm) and H_{Des} = 2.85 m. This yields to a specific speed of nq = 26.62, using the rotating speed in rpm, the flow rate in m³/s, and the head in m (or 1374.40 using rotating speed in rpm, the flow rate in US gpm, and head in feet).

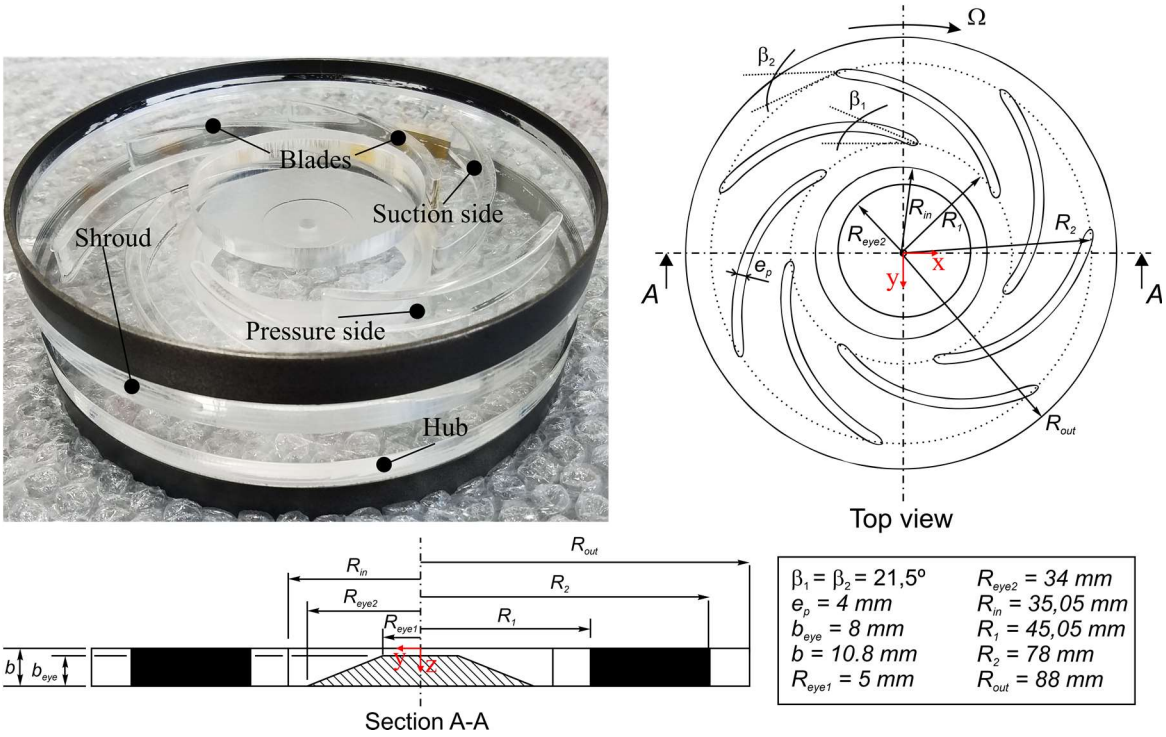

Figure 2 – Geometry of the rotor test with its main dimensions.

2.1 PIV system and acquisition procedure

Figure 3 shows details of the experimental circuit, where (a) presents a scheme of the test section and (b) a picture of the setup. The position of the PIV setup is also shown, mainly consisting of a laser, a camera, and an acquisition/processing system. An Nd: Yag double pulsed laser (532nm and 1060nm wavelength) with a maximum output power of 145 mJ was employed. An optical arrangement generates a laser sheet with approximately 1.2 mm in thickness. Neutrally buoyant hollow glass spheres varying from 9 to 13 μm are used as particle tracers. The camera used for image acquisition has a resolution of 2448x2050 pixels and is positioned 90 degrees above the rotor, 475 mm far from the hub, and 500.4 mm from the midplane between hub and shroud. A Nikkon® 50 mm lens equipped with a polarizing filter is used to reduce light scattering from the blades and reflecting surfaces.

The velocity fields were obtained by employing the phase-locking technique, and 500 pairs of images were acquired to ensure a robust data set and guarantee convergence in vector calculation. For this purpose, an electronic trigger device was located in the rotating shaft, as shown in Fig. 3, where the image is acquired in each impeller rotation. In this way, the camera and laser operation were synchronized, allowing to obtain images in a fixed position of the rotor channels.

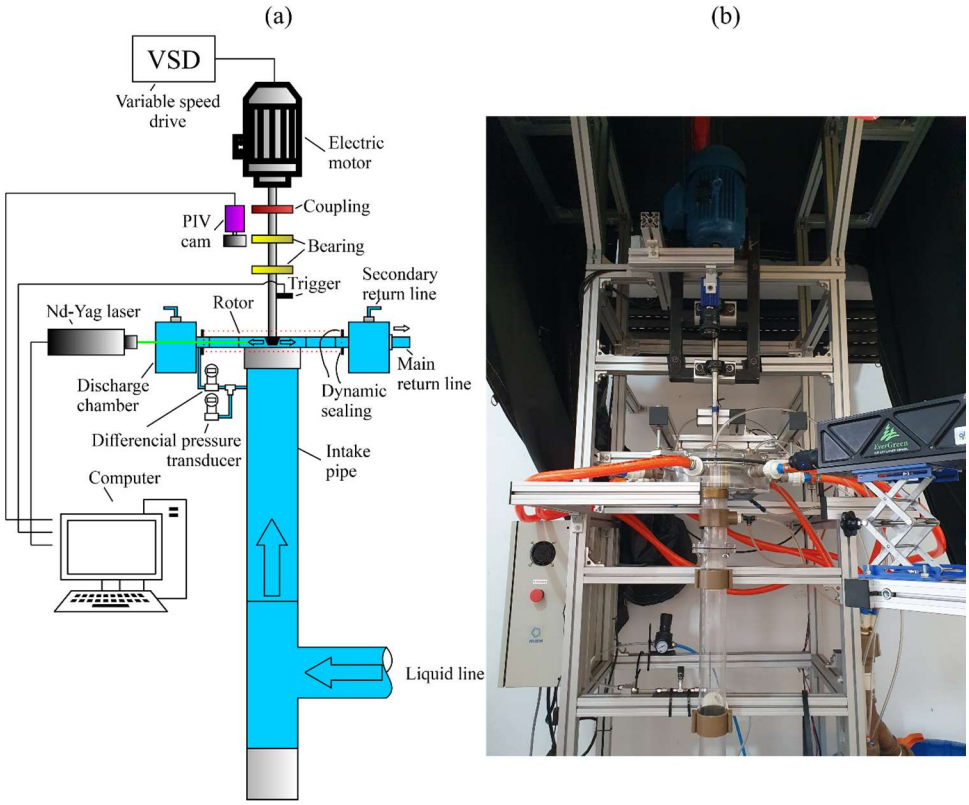

Figure 3 – Details of the experimental circuit: (a) schematic of the test section. (b) picture of the setup.

2.2 PIV processing

The images acquired by the PIV system were calibrated using a grid plate with dots of 1 mm in diameter and 8 mm in space between each point. The calibration target was placed at the shroud shown in Fig. 4. The calibration plate can correct distortions of the image, mainly near the border where the distortions are higher than the center.

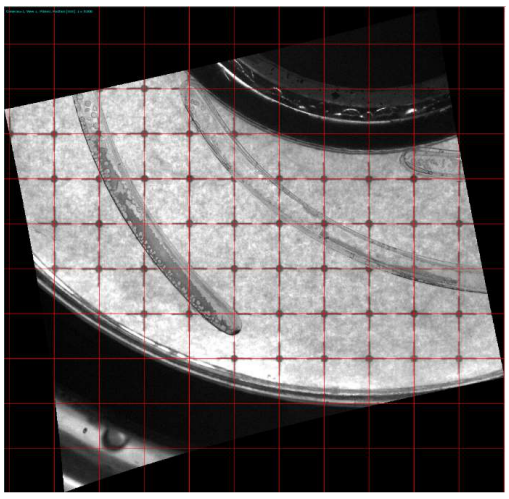

Figure 4 – Calibration image using a calibration plate with 1 mm diameter points and 8 mm space between each point.

Figure 5 illustrates the image processing procedure. Firstly, raw images were acquired (Fig. 5-(a)). Then, a masking procedure is applied to limit the flow region and remove out-of-interest sections of the images (Fig. 5-(b)). Next, a sliding average filter based on a Gaussian profile (Lukin, 2007) is applied (Fig. 5-(c)), improving the particles detection and then cross-correlation computations. Calculation of the velocity vectors was performed by applying a multi-pass approach. Initially, windows of 64x64 pixel² with 50% overlap were employed, then two additional calculations with window sizes of 16x16 pixel² without overlap were used. A median filter was applied twice after each pass and at the end of the last

step of processing. Interrogation windows that resulted in spurious and no vector regions were filled and/or substituted with vectors calculated by averaging the values of neighbor windows. An example of the instantaneous velocity calculation is shown in Fig. 5-(d).

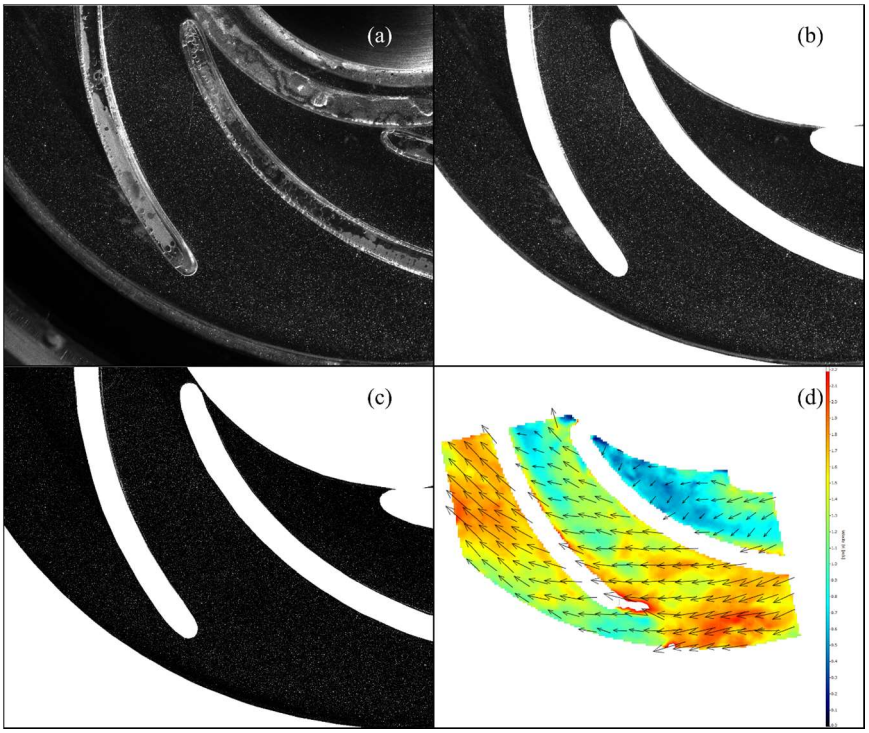

Figure 5 – PIV processing schematics. (a) raw image, (b) geometric mask, (c) sliding average filter, and (d) instantaneous velocity field.

After processing the images and obtaining the instantaneous velocity components ($u_i(x,y)$; $v_i(x,y)$), represented by Eq. (2), the mean velocity is calculated ($\bar{u}(x,y)$; $\bar{v}(x,y)$ by Eq. (3). The resulting absolute mean velocity is expressed by Eq. (4). The absolute velocity is not suitable for analyzing the flow in a rotating frame of reference because it also considers the system's rotating velocity. Therefore, the relative velocity is used instead, given by Eq. (5), where tangential velocity ($\vec{\Omega} \times \vec{r}$, which Ω is the angular velocity) at a given radius r was subtracted from the absolute velocity through a vector operation. The calculated relative velocity will be used in the following analysis and will be referred to as velocity for convenience.

$$u_i(x,y,t) = \bar{u}(x,y) + u_i'(x,y,t),\ v_i(x,y,t) = \bar{v}(x,y) + v_i'(x,y,t) \tag{2}$$

$$\bar{u}(x,y) = \frac{1}{N}\sum_{i=1}^{N} u_i(x,y,t),\ \bar{v}(x,y) = \frac{1}{N}\sum_{i=1}^{N} v_i(x,y,t) \tag{3}$$

$$\bar{C} = \bar{u}(x,y)\vec{i} + \bar{v}(x,y)\vec{j} \tag{4}$$

$$\vec{W} = \vec{C} - \vec{\Omega} \times \vec{r} \tag{5}$$

The turbulence kinetic energy is calculated assuming turbulence isotropy in the z-direction, which is calculated as the mean of the other two components (Sinha and Katz, 2000). Then, the turbulence kinetic energy is obtained by:

$$k = \frac{3}{2}\frac{1}{N}\sum_{i=1}^{N}\left[\frac{1}{2}u_i'^2(x,y,t) + \frac{1}{2}v_i'^2(x,y,t)\right] \tag{6}$$

The DaVis® software calculates the uncertainty based on the works of Wieneke (2015) and Sciacchitano and Wieneke (2016). The uncertainty for velocity, turbulence kinetic energy, and Reynolds shear stress were about 1%, 6%, and 8%, respectively.

2.3 Experimental test conditions

The present investigation was conducted in the following way. First, the head curve for different rotating speeds is presented to show that the head behaves according to similarity laws. Then, measurements at the midspan (z/b = 0.5) were conducted for different flow rates and rotating speeds. The goal was to evaluate the kinetic similarity expected in a centrifugal rotor. Finally, the focus of the work is shifted to evaluating the flow fields in different planes for 300 rpm rotating speed. As previously mentioned, four planes were chosen to perform this study, z/b = 0.2, 0.4, 0.6, and 0.8, where z/b = 0 corresponds to the hub wall and z/b = 1 is the shroud wall.
Table 1 presents the experimental conditions used in this work. The Q_{BEP} (flow rate at the Best Efficiency Point operation) was calculated using the similarity law based on the Q_{Des}. The BEP flow rate for 200, 300, 400, and 500 are respectively 2.45, 3.68, 4.91, and 6.14 m³/h.

z/b = 0.5								
Rotating speed [rpm]	Flow rate [Q/Q_{BEP}]							
200	0.25	0.50	0.75	1.00	1.25	1.50	1.75	2.00
300	0.25	0.50	0.75	1.00	1.25	1.50	1.75	2.00
400	0.25	0.50	0.75	1.00	1.25	1.50	1.75	2.00
500	0.25	0.50	0.75	1.00	1.25	1.50	1.75	2.00
z/b = 0.2, 0.4, 0.6, 0.8								
Rotating speed [rpm]	Flow rate [Q/Q_{BEP}]							
300	0.25	0.50	0.75	1.00	1.25	1.50	1.75	2.00

3. RESULTS

This section presents the results obtained in this work. The velocity flow fields were made dimensionless by the tangential velocity at D_{out} ($2 \cdot R_{out}$), while the turbulence kinetic energy is made dimensionless by taking the square root and dividing it by the tangential velocity. It is usually called turbulence intensity (Stel et al., 2013).

3.1 Head coefficient curves

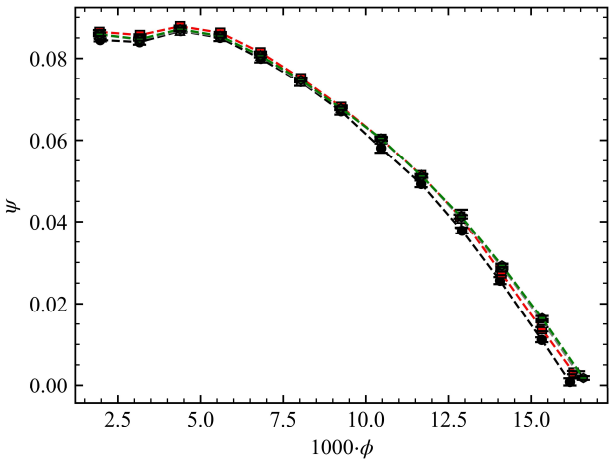

Figure 6 – Head coefficient as a function of flow coefficient for different rotating speeds.

Figure 6 presents the head coefficient $\left(\psi = gH / \Omega^2 D_{out}^2\right)$ as a function of the flow coefficient $\left(\phi = Q / \Omega D_{out}^3\right)$, measured for different rotating speeds. The curves reveal the usual pump head behavior, where the head coefficient decreases with an increasing flow coefficient. In addition, it can be observed that different rotating speeds produce similar curves, showing that the rotor prototype respects the pump`s similarity laws.

3.2 Flow pattern in different planes

In this section, results for three flow rates varying from $0.25 \cdot Q_{BEP}$ to $1.75 \cdot Q_{BEP}$ are presented in different planes for 300 rpm rotating speed. Four planes between hub ($z/b = 0$) and shroud ($z/b = 1$) at distances $z/b = 0.2$, 0.4, 0.6, and 0.8 are considered. The investigation starts with the Q_{BEP} case being the standard for comparison. Then, one over-load and one part-load condition are analyzed.

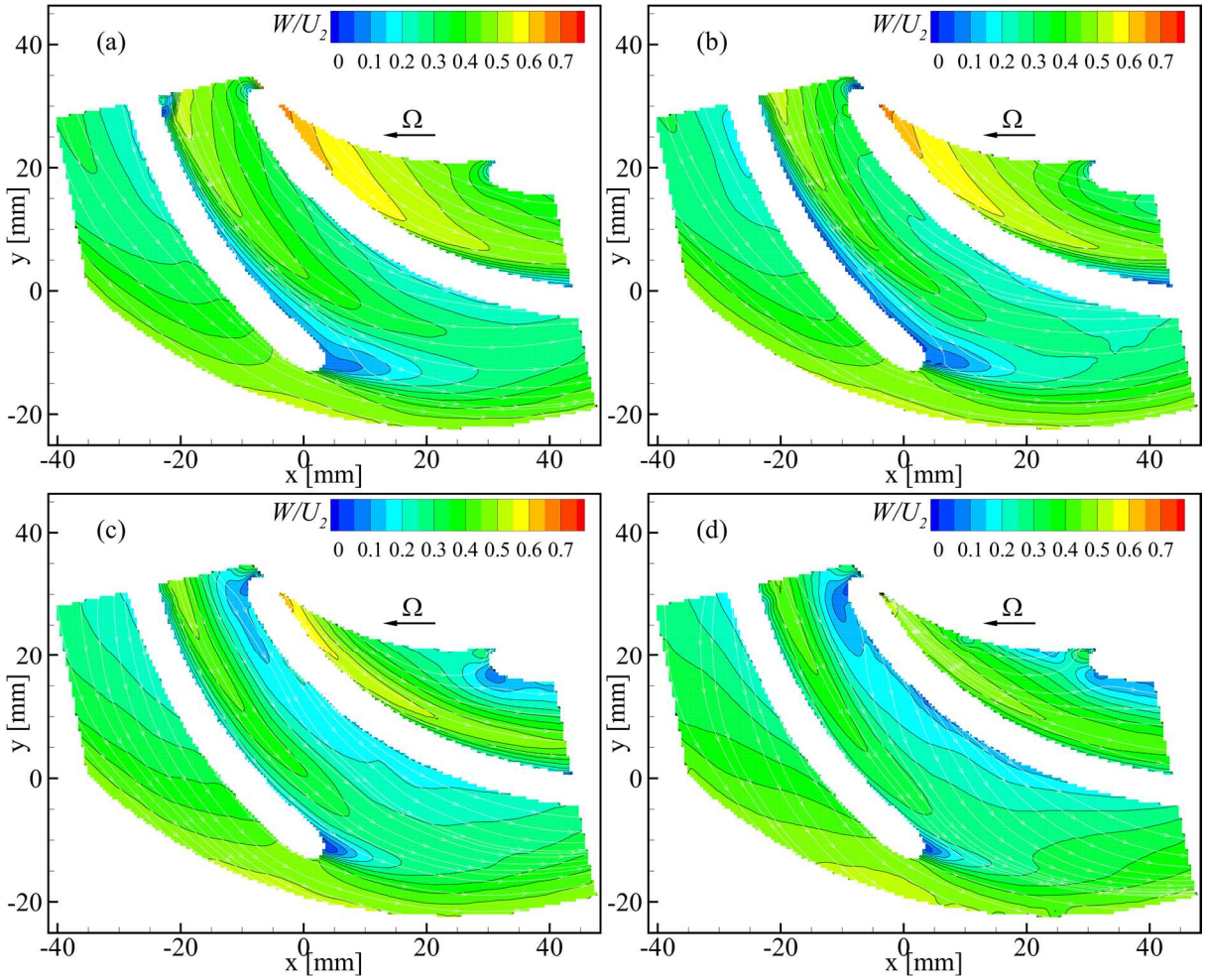

Figure 7 – Dimensionless velocity flow fields with streamlines for $1.00 \cdot Q_{BEP}$ at different planes, (a) z/b = 0.2, (b) z/b = 0.4, (c) z/b = 0.6, and (d) z/b = 0.8.

Figure 7 presents the dimensionless velocity flow fields with streamlines for $1.00 \cdot Q_{BEP}$ at four different planes. It can be noticed that the flow is oriented with the blade geometry in all four planes. Moreover, a jet-wake structure is observed near the blade tip, where a high velocity from the blade pressure side and a low velocity from the blade suction side interact downstream. In addition, it is observed that this structure increases from shroud to hub, which could indicate a higher slip near the hub than the shroud. Furthermore, velocity increases from shroud to hub near the inlet due to a change of flow direction from axial to radial that pushes the liquid towards the outer side (hub) because of centrifugal force.

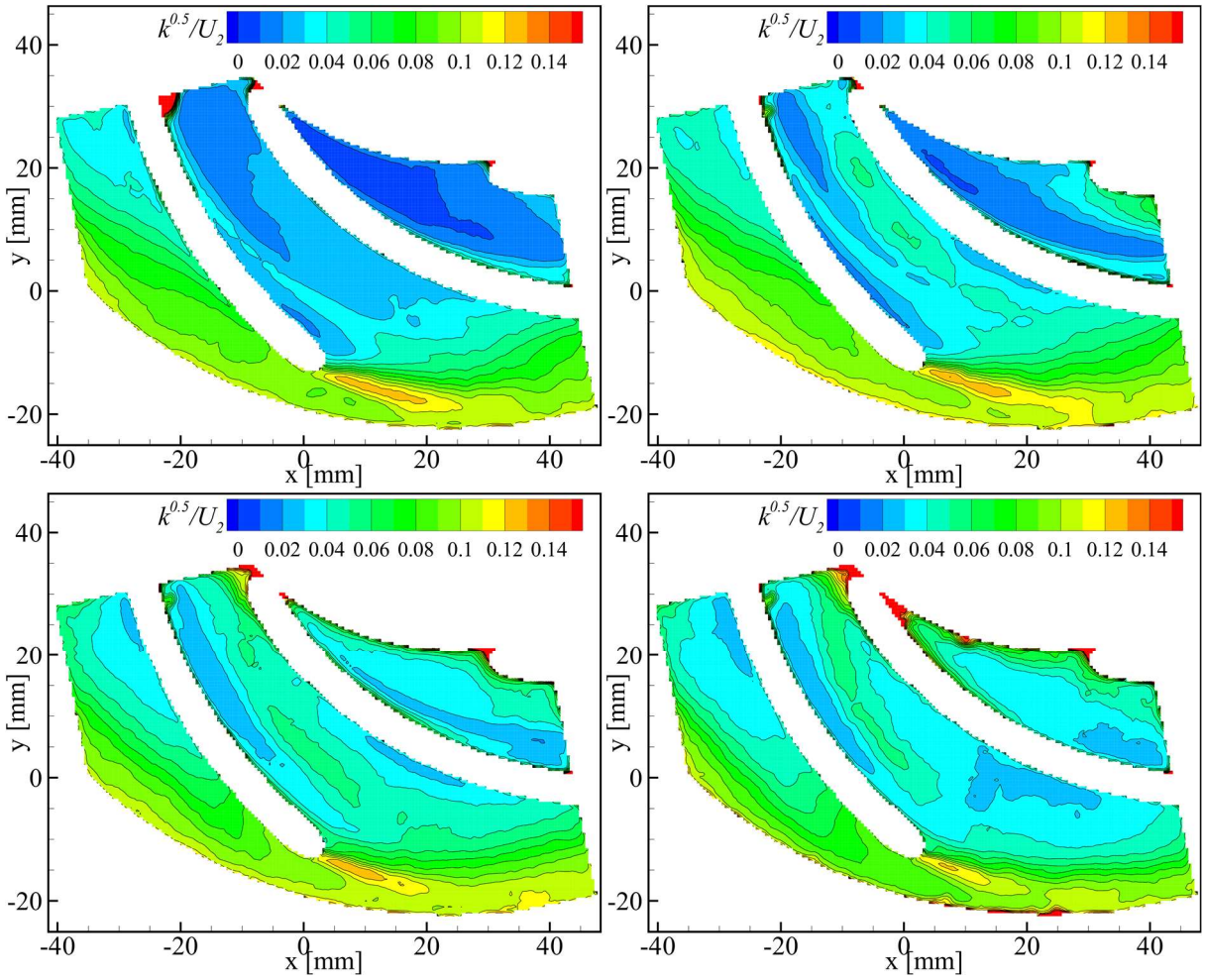

Figure 8 – Turbulence intensity fields for 1.00· Q_{BEP} at different planes, (a) z/b = 0.2, (b) z/b = 0.4, (c) z/b = 0.6, and (d) z/b = 0.8.

Figure 8 shows the turbulence intensity fields for 1.00·Q_{BEP} for four different planes. It can be observed that in the middle of the impeller channel, the turbulence is lower at plane (a) in comparison to the other planes. On the other hand, the turbulence near the rotor inlet is higher in planes (c) and (d) owing to a change in the flow direction. Moreover, near the blade tip, there is an increase in turbulence caused by the jet-wake structure, which is a bit longer in planes (a) and (b).

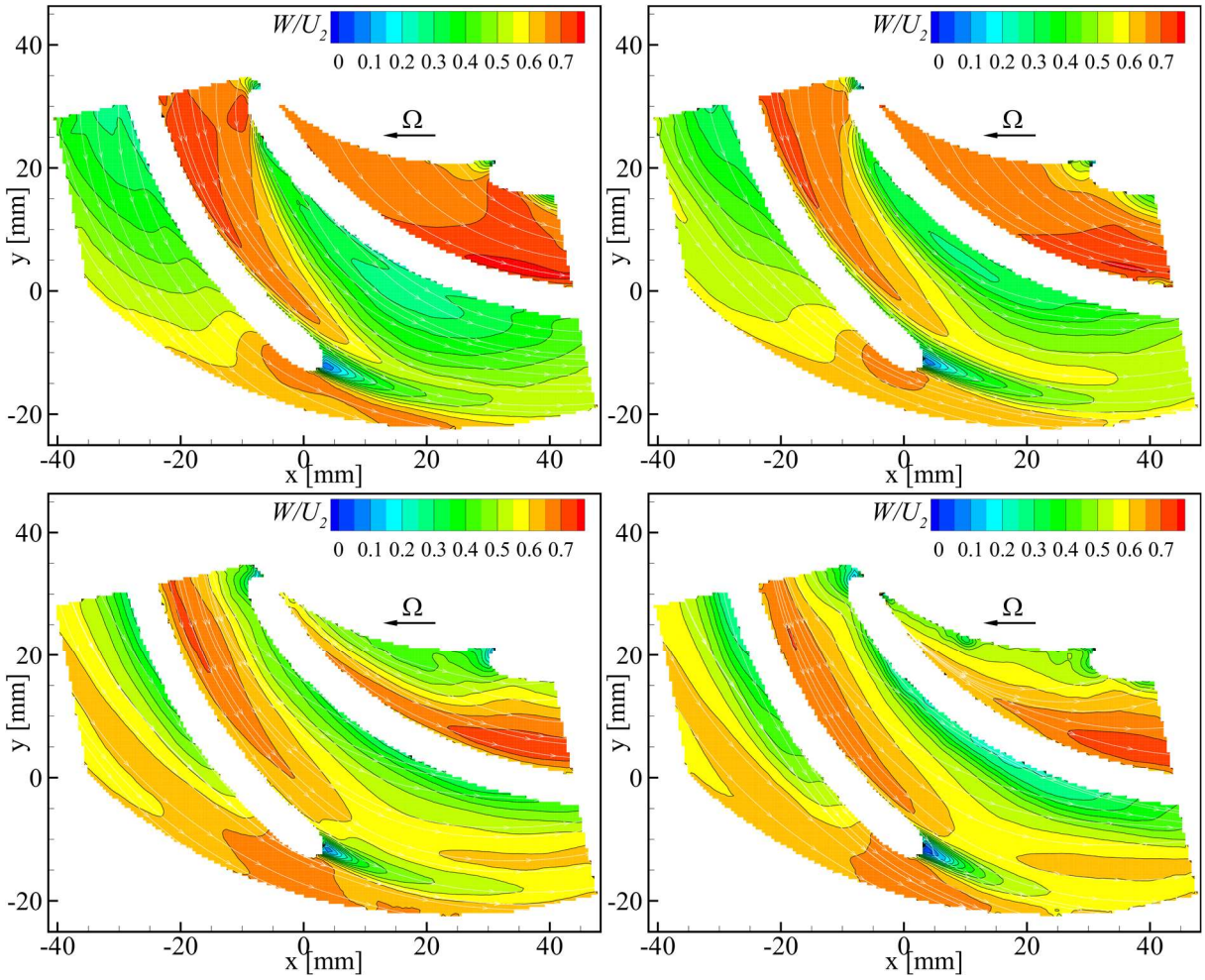

Figure 9 – Dimensionless velocity flow fields with streamlines for 1.75·Q_{BEP} at different planes, (a) z/b = 0.2, (b) z/b = 0.4, (c) z/b = 0.6, and (d) z/b = 0.8.

Figure 22 presents the dimensionless velocity flow fields with streamlines for 1.75· Q_{BEP} at four different planes. It can be observed that the streamlines are blade oriented, but their angle near the rotor exit has increased compared to Figs. 14 and 18. Near the inlet, the velocity increases from shroud to hub, while near the blade trailing edge tip and rotor exit, the velocity flow field is similar for all planes, including the jet-wake structure. Differently from what was observed in previous flow rates, a boundary layer separation seems to occur in the blade leading edge tip that is more pronounced in planes (a) and (b), which could be related to an increase in the flow angle at the leading edge tip.

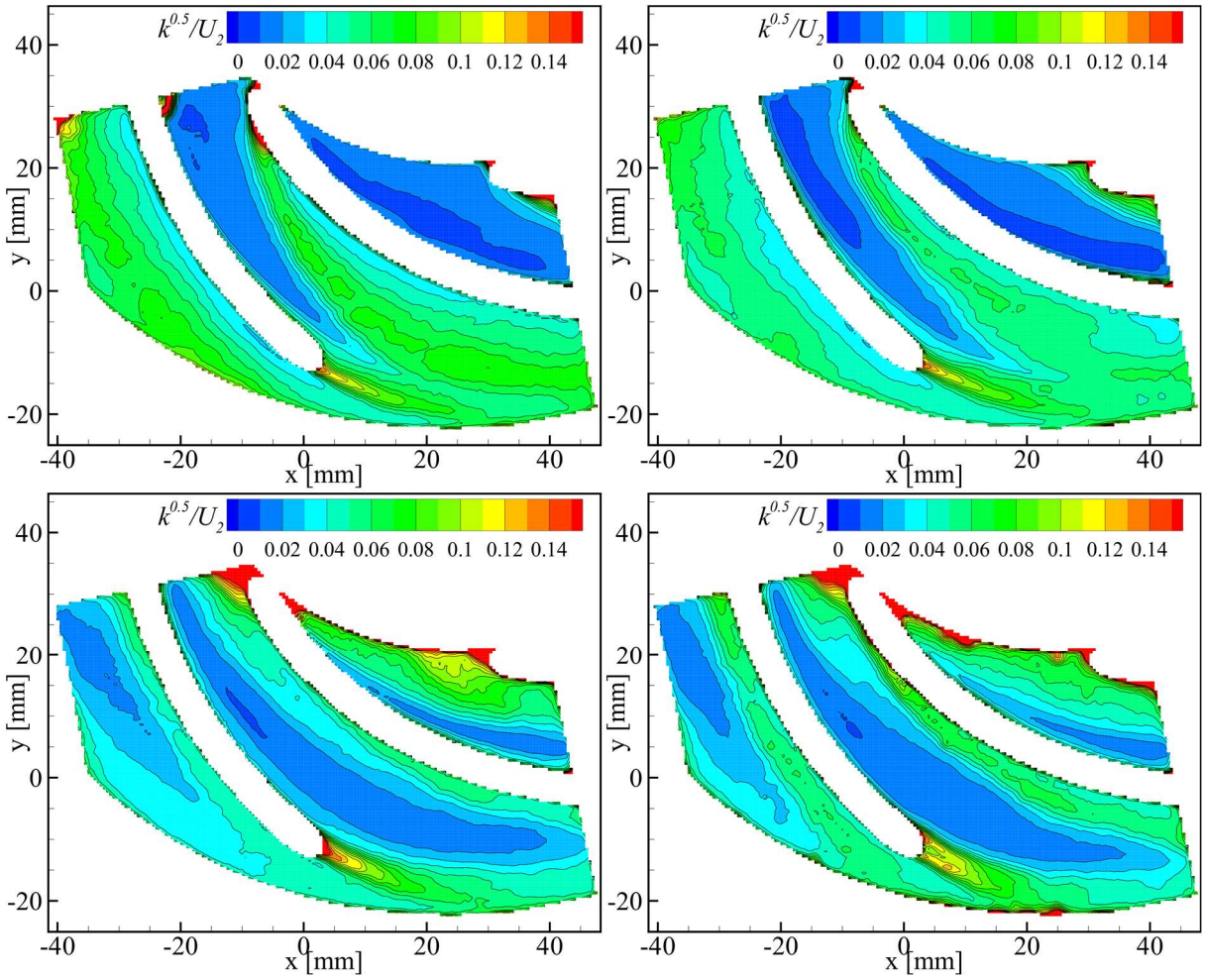

Figure 10 – Turbulence intensity fields for 1.75· Q_{BEP} at different planes, (a) z/b = 0.2, (b) z/b = 0.4, (c) z/b = 0.6, and (d) z/b = 0.8.

Figure 10 shows turbulence intensity fields for 1.75· Q_{BEP} at different planes. It can be noticed that the turbulence intensity diminishes from the hub to the shroud. Moreover, the turbulence in planes (a) and (b) has increased relative to 1.00·Q_{BEP}, suggesting that this increase is a consequence of flow rate increase. However, in planes (c) and (d), the turbulence has surprisingly decreased from 1.00· Q_{BEP} in the middle of the channel, although it is higher near the rotor inlet owing to a change of flow direction.

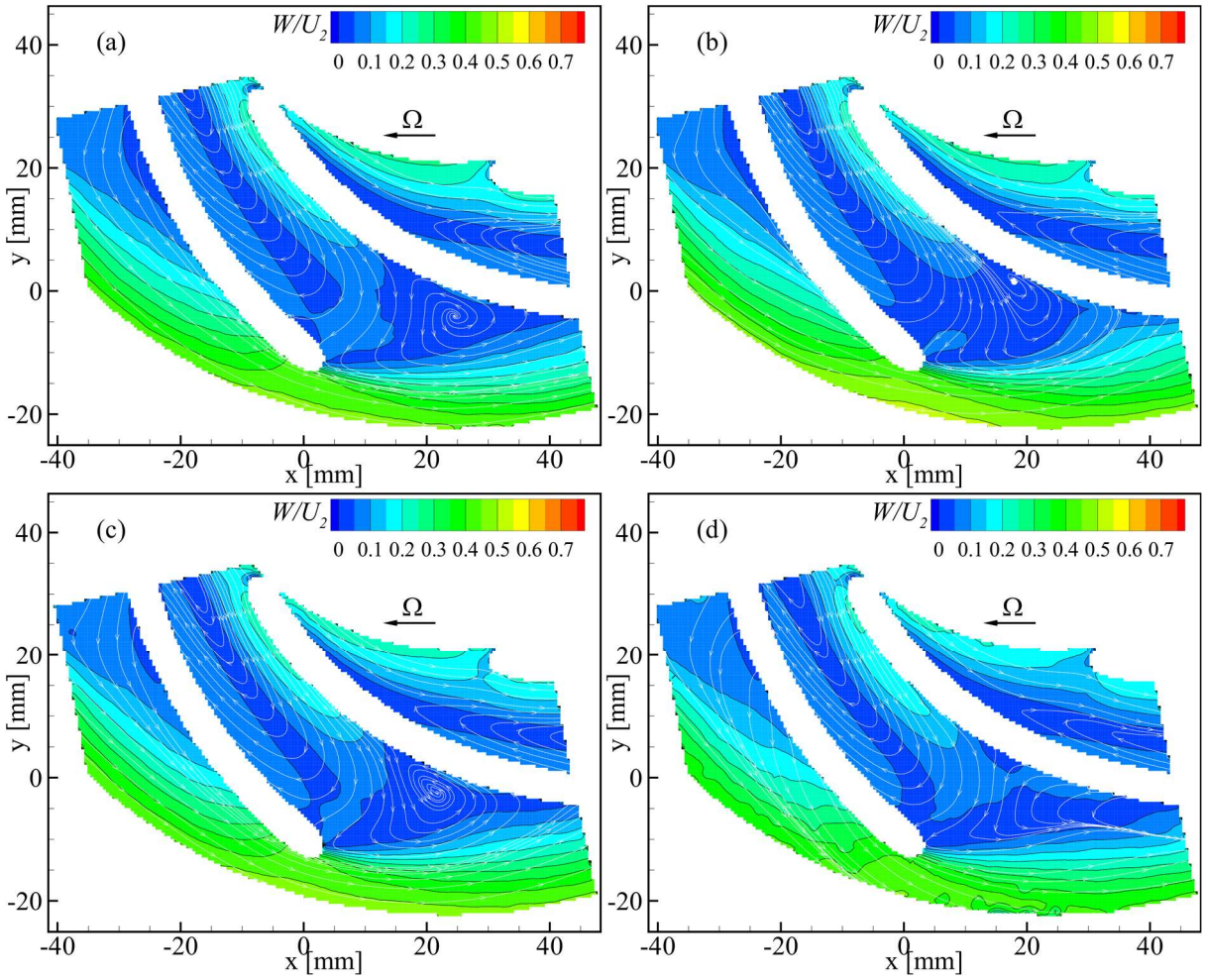

Figure 11 – Dimensionless velocity flow fields with streamlines for 0.25·Q_{BEP} at different planes, (a) z/b = 0.2, (b) z/b = 0.4, (c) z/b = 0.6, and (d) z/b = 0.8.

Figure 11 shows the dimensionless velocity flow field for 0.25· Q_{BEP} at different planes, (a) z/b = 0.2, (b) z/b = 0.4, (c) z/b = 0.6, and (d) z/b = 0.8. It can be observed that the flow pattern has completely changed. The stall cell has increased owing to an increase in incidence angle that starts flow separation near the rotor inlet. The velocity near the inlet is similar in all planes showing that the change of flow direction does not influence the intake velocity as previously observed. Moreover, the decrease of flow angle near the rotor exit has caused the formation of a secondary flow observed near the rotor outlet and the blade pressure side that counteracts the impeller rotation. This secondary flow has been observed in other works (Feng et al., 2009; Li et al., 2020) but in a midspan plane.

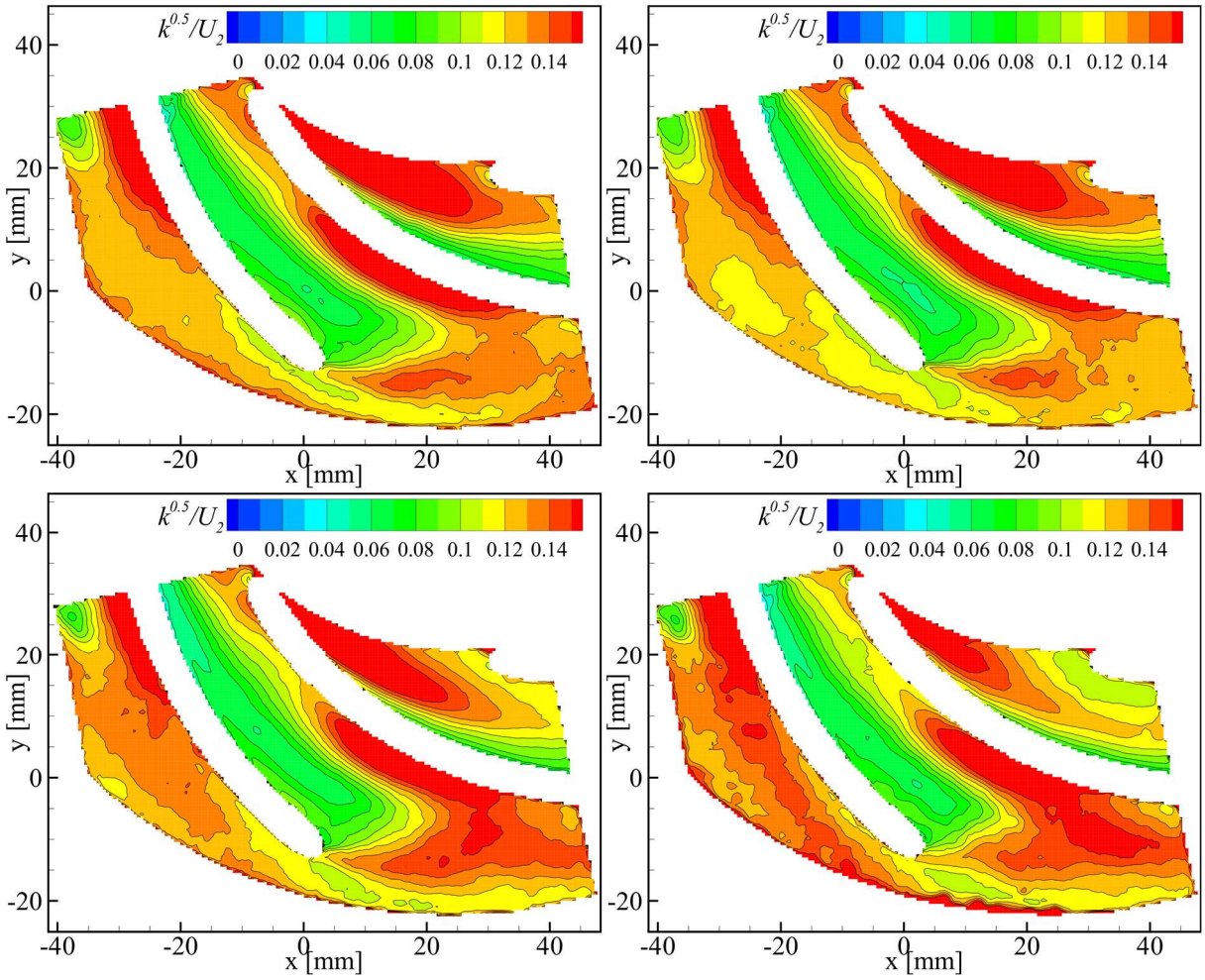

Figure 12 – Turbulence intensity fields for 0.25· Q_{BEP} at different planes, (a) z/b = 0.2, (b) z/b = 0.4, (c) z/b = 0.6, and (d) z/b = 0.8.

Figure 12 presents turbulence intensity fields for 0.25· Q_{BEP} at different planes. High turbulence kinetic energy regions are observed in all planes. Note that there is high turbulence intensity in the region of the small stall cell. Moreover, there is high turbulence in the pressure side between the two stall cells, which could indicate that the turbulence is due to an interaction between the two stall cells. Lower turbulence is found near the blade suction side that roughly corresponds to the stall cell region, indicating that the bigger stall cell is relatively more stable than the secondary stall cell. Again, differences between planes are also not clearly apparent.

In general, the flow field investigation in different planes has shown that the flow near the hub differs from the flow near the shroud. For flow rates higher than 1.00· Q_{BEP} the velocity near the hub is higher than near the shroud due to a change of flow direction (axial to radial). Moreover, turbulence is higher near the inlet for planes (c) and (d) owing to a change of flow direction. Turbulence is carried throughout the impeller channels up to the middle of the channel, where it is damped. For part-load operation, stall cell formation was observed due to flow separation near the leading edge tip, and a secondary flow occurred near the blade pressure side and rotor exit. Furthermore, no significant changes were observed between planes for the variables analyzed at this flow rate operation.

4. CONCLUSION

This work has presented an analysis of the flow field in a centrifugal rotor for different flow rates and rotating speeds. PIV measurements were performed at different planes (z/b = 0.2, 0.4, 0.5, 0.6, and 0.8). The main conclusions are as follows:

i. The pressure rise curves have shown to follow the similarity expected for centrifugal pumps.

ii. From the analysis of the flow in different planes, it could be observed that only for 0.25· Q_{BEP} the flow field in all planes were similar. For flow rates higher than 0.25· Q_{BEP} the velocity magnitudes and turbulence intensities were distinct in different planes. The difference in the flow fields in different planes is mainly caused by the change in the flow direction from the development pipe to the rotor channels.

iii. At part-load operations, the rotational effect on the flow field is dominant. Stall cells were found in the impeller channels for $0.25 \cdot Q_{BEP}$. Moreover, turbulence intensities is higher than in BEP or over-load conditions due to flow pattern change.

5. ACKNOWLEDGMENTS

The authors acknowledge the financial support of CAPES foundation.

6. REFERENCES

Feng, J., Benra, F.K., Dohmen, H.J., 2010a. "Unsteady flow investigation in rotor-stator interface of a radial diffuser pump". *Forschung im Ingenieurwesen*, 74, 233–242. https://doi.org/10.1007/s10010-010-0128-x

Feng, J., Benra, F.K., Dohmen, H.J., 2010b. "Application of different turbulence models in unsteady flow simulations of a radial diffuser pump". *Forschung im Ingenieurwesen*, 74, 123–133. https://doi.org/10.1007/s10010-010-0121-4

Feng, J., Benra, F.K., Dohmen, H.J., 2009. "Unsteady flow visualization at part-load conditions of a radial diffuser pump: By PIV and CFD". *Journal of Visualization*, 12, 65–72. https://doi.org/10.1007/BF03181944

Keller, J., Blanco, E., Barrio, R., Parrondo, J., 2014. "PIV measurements of the unsteady flow structures in a volute centrifugal pump at a high flow rate". *Experiments in Fluids,* 55. https://doi.org/10.1007/s00348-014-1820-7

Li, W., Zhou, L., Shi, W. dong, Ji, L., Yang, Y., Zhao, X., 2017. "PIV experiment of the unsteady flow field in mixed-flow pump under part loading condition". *Experimental Thermal and Fluid Science*, 83, 191–199. https://doi.org/10.1016/j.expthermflusci.2017.01.009

Li, X., Chen, H., Chen, B., Luo, X., Yang, B., Zhu, Z., 2020. "Investigation of flow pattern and hydraulic performance of a centrifugal pump impeller through the PIV method". *Renewable Energy*, 162, 561–574. https://doi.org/10.1016/j.renene.2020.08.103

Ofuchi, E.M., Stel, H., Sirino, T., Vieira, T.S., Ponce, F.J., Chiva, S., Morales, R.E.M., 2017. "Numerical investigation of the effect of viscosity in a multistage electric submersible pump". *Engineering Applications of Computational Fluid Mechanics*, 11, 258–272. https://doi.org/10.1080/19942060.2017.1279079

Pedersen, N., Larsen, P.S., Jacobsen, C.B., 2003. "Flow in a centrifugal pump impeller at design and off-design conditions - Part I: Particle image velocimetry (PIV) and laser Doppler velocimetry (LDV) measurements". *Journal of Fluids Engineering*, ASME 125, 61–72. https://doi.org/10.1115/1.1524585

Posa, A., Lippolis, A., 2019. "Effect of working conditions and diffuser setting angle on pressure fluctuations within a centrifugal pump". *International Journal of Heat and Fluid Flow*, 75, 44–60. https://doi.org/10.1016/j.ijheatfluidflow.2018.11.011

Si, Q., Ali, A., Yuan, J., Fall, I., Muhammad Yasin, F., 2019. "Flow-Induced Noises in a Centrifugal Pump: A Review". *Science of Advanced Materials*. 11, 909–924. https://doi.org/10.1166/sam.2019.3617

Sinha, M., Katz, J., Meneveau, C., 2000. "Quantitative Visualization of the Flow in a Centrifugal Pump With Diffuser Vanes—II: Addressing Passage-Averaged and Large-Eddy Simulation Modeling Issues in Turbomachinery Flows". *Journal of Fluids Engineering*, 122, 108–116. https://doi.org/10.1115/1.483232

Sinha, M., Pinarbasi, A., Katz, J., 2001. "The flow structure during onset and developed states of rotating stall within a vaned diffuser of a centrifugal pump". *Journal of Fluids Engineering*, ASME 123, 490–499. https://doi.org/10.1115/1.1374213

Stel, H., Amaral, G.D.L., Negrão, C.O.R., Chiva, S., Estevam, V., Morales, R.E.M., 2013. "Numerical analysis of the fluid flow in the first stage of a two-stage centrifugal pump with a vaned diffuser". *Journal of Fluids Engineering,* ASME 135, 1–9. https://doi.org/10.1115/1.4023956

Stel, H., Ofuchi, E.M., Alves, R.F., Chiva, S., Morales, R.E.M., 2020a. "Experimental Analysis of Gas–Liquid Flows in a Centrifugal Rotor". *Journal of Fluids Engineering,* 142. https://doi.org/10.1115/1.4045857

Stel, H., Ofuchi, E.M., Chiva, S., Morales, R.E.M., 2020b. "Numerical simulation of gas-liquid flows in a centrifugal rotor". *Chemical Engineering Science*, 221, 115692. https://doi.org/10.1016/j.ces.2020.115692

Stel, H., Sirino, T., Ponce, F.J., Chiva, S., Morales, R.E.M., 2015. "Numerical investigation of the flow in a multistage electric submersible pump". *Journal of Petroleum Science and Engineering*, 136, 41–54. https://doi.org/10.1016/j.petrol.2015.10.038

Tong, Z. ming, Xin, J. ge, Tong, S. guang, Yang, Z. qin, Zhao, J. yun, Mao, J. hua, 2020. "Internal flow structure, fault detection, and performance optimization of centrifugal pumps". *Journal of Zhejiang University-SCIENCE (Applied Physics & Engineering)*, 21, 85–117. https://doi.org/10.1631/jzus.A1900608

Vieira, T.S., Siqueira, J.R., Bueno, A.D., Morales, R.E.M., Estevam, V., 2015. "Analytical study of pressure losses and fluid viscosity effects on pump performance during monophase flow inside an ESP stage". *Journal of Petroleum Science and Engineering*, 127, 245–258. https://doi.org/10.1016/j.petrol.2015.01.014

Zhang, N., Gao, B., Li, Z., Ni, D., Jiang, Q., 2018. "Unsteady flow structure and its evolution in a low specific speed centrifugal pump measured by PIV". *Experimental Thermal and Fluid Science*, 97, 133–144. https://doi.org/10.1016/j.expthermflusci.2018.04.013

7. RESPONSIBILITY NOTICE

The author(s) is (are) the only responsible for the printed material included in this paper.